RSC Advances

PAPER

View Article Online
View Journal | View Issue

Check for updates

Cite this: *RSC Adv.*, 2018, **8**, 39837

Mn substituted $Mn_xZn_{1-x}Co_2O_4$ oxides synthesized by co-precipitation; effect of doping on the structural, electronic and magnetic properties†

Tarekegn Heliso Dolla,[a] David G. Billing,[b] Charles Sheppard,[c] Aletta Prinsloo,[c] Emanuela Carleschi,[d] Bryan P. Doyle,[d] Karin Pruessner[e] and Patrick Ndungu *[a]

Received 1st October 2018
Accepted 20th November 2018

DOI: 10.1039/c8ra08150f

rsc.li/rsc-advances

Mn substituted $Mn_xZn_{1-x}Co_2O_4$ ($x = 0, 0.3, 0.5, 0.7, 1$) oxides were synthesized by a facile co-precipitation method followed by calcination at 600 °C. The presence of manganese ions causes appreciable changes in the structural and magnetic properties of the Mn-substituted $ZnCo_2O_4$. The morphologies, structures, and electronic properties of Mn–Zn–Co oxide microspheres were characterized using scanning electron microscopy, transmission electron microscopy, X-ray diffraction, Fourier transform infrared spectroscopy, and X-ray photoelectron spectroscopy. The X-ray diffraction and Fourier transform infrared spectroscopy results confirmed the formation of spinel $Mn_xZn_{1-x}Co_2O_4$. It was shown that the Mn–Zn–Co oxide microspheres increase in size and become regular in shape with increasing Mn concentration with the crystal size lying in the range from 19.1 nm to 51.3 nm. Magnetization measurements were carried out using a vibrating sample magnetometer at room temperature and 10 K. The saturation magnetization is observed to increase with increasing Mn concentration from $x = 0$ to $x = 1$.

1. Introduction

Nano-structured spinel-type transition metal oxides have been investigated intensively for various potential applications including chemical sensors,[1,2] energy storage devices,[3] pigments,[4] catalysts[5] and spintronics.[6–8] Among the various transition metal oxides, spinel-type $ZnCo_2O_4$ has attracted much attention as an important p-type semiconductor; which has been used as an anode material in lithium ion batteries,[9] in gas sensors,[2,10] organic photovoltaics, electrocatalysis,[11] photocatalysis,[12,13] and as a p-type gate in junction field-effect transistors.[14]

The magnetic properties of Zn–Co–O systems have been widely investigated, with a number of studies focusing on the thin films and powders, which have exhibited properties ranging from paramagnetic to strong ferromagnetic behaviour.[15–18] Several studies have shown that room temperature ferromagnetism is observed in Zn based transition metal oxide systems such as Zn–Co–O and Zn–Co–Mn–O[19] because of an exchange interaction mechanism such as double-exchange, super-exchange and through dopant electron-delocalized conduction band electron interactions.[20,21] The ferromagnetism of spinel-type $ZnCo_2O_4$ is a continuous debate and its microscopic origins remain poorly understood. Its ferromagnetism is believed to arise due to hole mediated Co–Co interaction while the behaviour turns out to be antiferromagnetic as a result of Co–O–Co super exchange interaction,[22] which also exhibits magnetoresistance effect and have application as promising materials for spintronics.[23,24] Kim *et al.*[22,25] have investigated the electrical and magnetic properties of spinel-type p-type semiconducting $ZnCo_2O_4$ thin films, with results suggesting that departure from stoichiometry in this compound affects its electrical and magnetic properties.

The $ZnCo_2O_4$ structure has remarkable features in that it forms a regular spinel structure where Zn^{2+} ions occupy tetrahedral (T_h) sites and the Co^{3+} and Co^{2+} ions in octahedral (O_h) and some in tetrahedral sites.[26,27] The variation in the magnetic properties of a $ZnCo_2O_4$ can arise when there is a substitution of nonmagnetic ions by magnetic ions. Many studies were conducted on Zn-based spinel oxides to demonstrate the effect of substitution of nonmagnetic ions on their magnetic and structural properties.[28–30] The studies have shown a significant change in the magnetic properties during substitution due to a predominant super-exchange interaction between the cations in the A-site and B-site *via* oxygen ions.

In the present study, we report the synthesis of $Mn_xZn_{1-x}Co_2O_4$ ($x = 0, 0.3, 0.5, 0.7$, and 1) employing a facile coprecipitation method. The structural, electronic and magnetic

---

[a] *Energy, Sensors and Multifunctional Nanomaterials Research Group, Department of Applied Chemistry, University of Johannesburg, Doornfontein Campus, South Africa. E-mail: pndungu@uj.ac.za*

[b] *DST-NRF Centre of Excellence in Strong Materials and Molecular Sciences Institute, School of Chemistry, University of the Witwatersrand, Johannesburg, South Africa*

[c] *Chromium Research Group, Department of Physics, University of Johannesburg, Auckland Park, South Africa*

[d] *Department of Physics, University of Johannesburg, Auckland Park, South Africa*

[e] *School of Chemistry and Physics, University of KwaZulu-Natal, Durban, South Africa*

† Electronic supplementary information (ESI) available. See DOI: 10.1039/c8ra08150f

properties of the nano-crystalline $Mn_xZn_{1-x}Co_2O_4$ in relation to the concentration of Mn were investigated.

2. Experimental

2.1 Chemicals

Analytical reagents of $Ni(Ac)_2 \cdot 4H_2O$, $Mn(Ac)_2 \cdot 4H_2O$ and $Co(Ac)_2 \cdot 4H_2O$ were obtained from Sigma-Aldrich. NH_4HCO_3 and absolute ethanol (≥99.8%) were purchased from Merck Millipore.

2.2 Materials synthesis

Mn substituted $Mn_xZn_{1-x}Co_2O_4$ was synthesized with a facile co-precipitation method followed by annealing. In a typical synthesis of $Mn_{0.5}Zn_{0.5}Co_2O_4$ ($x = 0.5$), 0.245 g of $Mn(Ac)_2 \cdot 4H_2O$, 0.22 g of $Zn(Ac)_2 \cdot 4H_2O$ and 0.996 g of $Co(Ac)_2 \cdot 4H_2O$ were dissolved in a mixture of 7 mL of ethanol and 70 mL of distilled water with vigorous stirring to form solution A. Then, 4.74 g of NH_4HCO_3 was dissolved in 70 mL of distilled water to form solution B, which was then added to solution A drop wise, while stirring. The resulting mixed solution was heated to 45 °C and maintained at this temperature for 9 h with vigorous stirring. A pale pink precipitate was obtained, which was collected through filtration, washed thoroughly with distilled water and ethanol and then dried at 60 °C overnight. The obtained carbonate precursor was heat treated in air at 600 °C for 5 h at a temperate ramp of 2 °C min^{-1} to yield a black powder.

2.3 Characterization

The phase components and structure of the as-prepared materials were characterized using Bruker D2 Phaser X-ray Diffractometer (XRD; Co Kα radiation, $\lambda = 1.78060$ Å). The XRD data for Rietveld refinement was measured using a D9 X-ray Diffractometer (XRD; Mo $K\alpha_1$ radiation, $\lambda = 0.709321$ Å) and was analyzed on TOPAS software (version 5). Fourier transform infrared (FTIR) spectra were recorded in the range of 4000–400 cm^{-1} using a Shimadzu 8400 FTIR spectrometer employing potassium bromide (KBr) pellets technique at room temperature. Morphology of the materials was obtained on FEI Nova Nano SEM 450 Scanning Electron Microscope (SEM) and JEOL 2100 Transmission Electron Microscopy (TEM). The composition of the samples was analyzed by EDX attached to the SEM instrument. Raman spectra were acquired at room temperature on a Thermo Scientific DXR2 Smart Raman equipped with a 532 nm laser source. The specific surface area was determined using Brunauer–Emmett–Teller (BET) technique and was determined from N_2 adsorption/desorption isotherms obtained on an ASAP 2020 (Micrometrics instrument, USA) surface area analyzer. Thermogravimetric Analysis (TGA) was carried out under airflow with a temperature ramp of 10 °C min^{-1} using Thermogravimetry/Differential Thermal Analyzer (Hitachi-STA7200RV, California, USA). Magnetic measurements were performed using a Cryogenic measurement platform equipped with a vibrating sample magnetometer (VSM) insert. VSM measurements were done in zero field cooled (ZFC) and field cooled (FC) modus of measurement in a temperature range of 2 to 300 K. Hysteresis loops were performed in a field range of +2.5 T to −2.5 T at two different temperatures of 10 K and 300 K. X-ray photoemission (XPS) spectra were performed at room temperature using a SPECS PHOIBOS 150 hemispherical electron energy analyser. The photon source used was a SPECS XR 50 M monochromatised X-ray source equipped with an Al Kα anode ($h\nu = 1486.71$ eV). The overall energy resolution was set to 0.7 eV for survey spectra and 0.55 eV for all other high-resolution core level spectra shown in this work. High resolution XPS spectra for $ZnCo_2O_4$ are not reported here. The reason for this is that the sample was too insulating for charge compensation to take place effectively, even with the aid of a flood gun. The line shape of the XPS spectra for this sample was therefore distorted, making the information extracted from them meaningless. We therefore report high resolution core level spectra only for the other four compounds in the $Mn_xZn_{1-x}Co_2O_4$ series ($x = 0$, 0.3, 0.5 and 0.7).

3. Results and discussion

3.1 Formation of the spinel-type oxides

With the starting chemical precursors, the formation reactions of the $Mn_xZn_{1-x}Co_2(CO_3)_2$ precursor can be described in the following two steps:

$$2NH_4HCO_3 \rightarrow H_2CO_3 + 2NH_4^+ + CO_3^{2-} \tag{1}$$

$$xMn^{2+} + (1-x)Zn^{2+} + 2Co^{2+} + 2CO_3^{2-} \rightarrow Mn_xZn_{1-x}Co_2(CO_3)_2 \tag{2}$$

The ammonium hydrogen carbonate used in the present synthesis mainly serves as a source for the generation of carbonate, as explained in eqn (1), while the divalent metal cations are obtained from the acetate precursors.

Thermal analysis allows for determining the precursor decomposition temperature during the heat treatment, which eventually will produce the oxide. Thermogravimetric (TG) and differential scanning calorimetric (DSC) analyses were performed to characterize the thermal properties and further determine the sintering temperature of the carbonate precursor. Fig. 1 shows the DSC and TG curves of the as prepared carbonate precursors

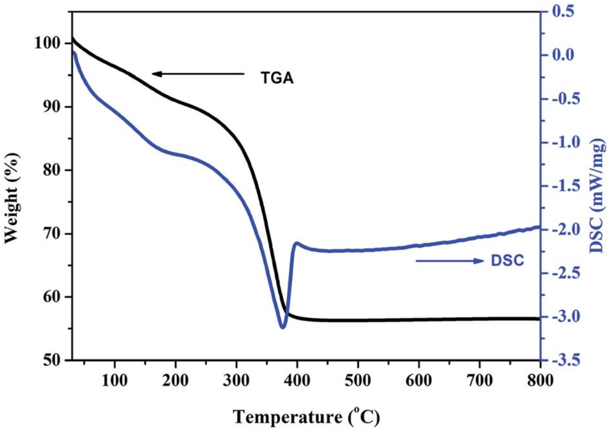

Fig. 1 Thermogravimetric (TG) and differential scanning calorimetry (DSC) analysis curves of the $Zn_{0.5}Mn_{0.5}Co_2CO_3$ precursor in an air atmosphere.

for the composition $x = 0.5$. It can be seen that the carbonate precursor decomposes in two steps. The first step occurs between 120 °C and 190 °C, which is indicated by a small exothermic peak on the DSC curve. It is due to the evaporation of water adsorbed on the surface of the precursor sample. In the second step, a major mass loss of 35% occurs between 196 °C and 430 °C, which can be attributed to the decomposition of the carbonate precursor to a metal oxide. The DSC curve shows a sharp exothermic peak at about 376 °C, corresponding to this dominant mass loss, which indicates that the amorphous carbonate precursor transformed to $Zn_{0.5}Mn_{0.5}Co_2O_4$ at this temperature.

3.2 Structural studies

Crystalline nature and phase identity of the prepared materials were precisely determined from X-ray diffraction (XRD) studies. The XRD patterns of the Mn doped $ZnCo_2O_4$, $Mn_xZn_{1-x}Co_2O_4$ ($x = 0, 0.3, 0.5, 0.7, 1$), oxides prepared by facile coprecipitation route and heat treatment at 600 °C are shown in Fig. 2.

The peaks at 2θ values are well matched with the standard cubic spinel structure of $ZnCo_2O_4$ (PDF card no. 23-1390) and $MnCo_2O_4$ (PDF card no. 23-1237) corresponding to the (111), (220), (311), (222), (400), (422), (511), and (440) lattice planes. This observation demonstrates the formation of a single phase for all the compositions. The intensity of the diffraction peaks of $Mn_xZn_{1-x}Co_2O_4$ increases and the peak width (full width at half maximum, FWHM) decreases with increasing Zn concentration. The crystallite size was observed to decrease irregularly from 51 to 19 nm with increasing Mn concentration. Rietveld analysis of the XRD pattern of $Mn_xZn_{1-x}Co_2O_4$ obtained from X-ray diffractometer with Mo-tube (see Fig. S-1† for XRD data using Mo, and Fig. S-2† for Rietveld refined patterns) is shown in Fig. 2(b) and the values are presented in Table 1 with the reliability factors (R_{wp}, R_B, GOF), lattice parameter and crystal size given.

The lattice parameter, $a = 8.0874$ Å, calculated for $ZnCo_2O_4$ is close to the reported values (PDF card no. 23-1390). On substituting Mn ions for Zn^{2+}, the lattice parameter increases compared to that of the pure $ZnCo_2O_4$ because of the slightly bigger ionic size of Mn ions compared to Zn^{2+} (0.740 Å).[31] The lattice parameter shows a clear increase and a linear behaviour with increase of Mn ion doping which further corroborates successful substitution by the Mn ion.

Raman spectra for all of the compositions were recorded at room temperature and are shown in Fig. 3. The samples displayed two broad peaks between 460–540 cm^{-1}, and 670–720 cm^{-1}. Typically spinel metal oxides such as $ZnCo_2O_4$ and $MnCo_2O_4$ display 5 active Raman modes. With $ZnCo_2O_4$ there are three F_{2g} modes which can occur around 190, 520, and 610 cm^{-1}, an E_g mode around 470 cm^{-1}, and an A_{1g} mode at 690 cm^{-1}.[32–34] The phonon modes (three F_{2g}, an E_g, and an A_{1g} mode) for $MnCo_2O_4$ occur at similar positions.[35] The broad peaks obtained obscure the various modes, and the broadness can be attributed to the nano-size of the materials (see TEM analysis section).

These characteristics peaks for crystalline spinel metal oxides can shift by several cm^{-1}, and can be ascribed to the change in the surface strain or defects owing to the incorporation of Mn into the $ZnCo_2O_4$ crystal structure.[32–35] The lack of distinct separate or characteristic peaks for the separate oxides are in accordance with the XRD results.

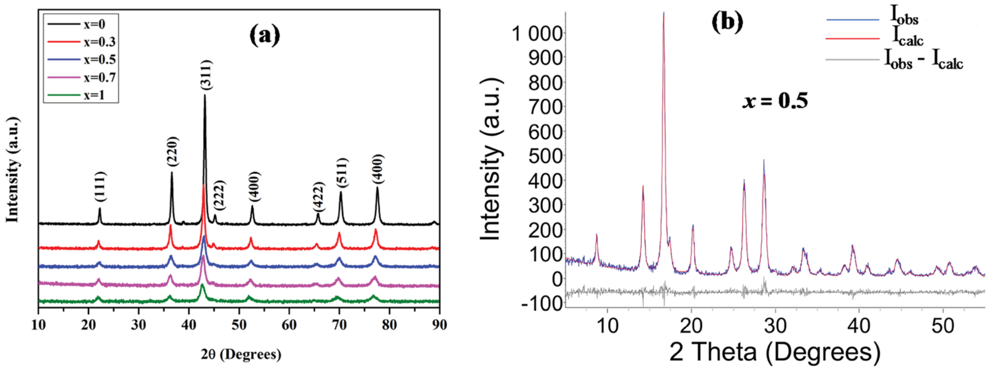

Fig. 2 Panel (a) XRD patterns of the Mn substituted $Mn_xZn_{1-x}Co_2O_4$ oxide with different Mn concentrations; $x = 0, 0.3, 0.5, 0.7$ and 1. Panel (b) Rietveld refined XRD pattern of $Mn_{0.5}Zn_{0.5}Co_2O_4$.

Table 1 Retiveld refined parameters for $Mn_xZn_{1-x}Co_2O_4$

Compound	Lattice parameter (a), Å	R_{wp} (%)	R_B (%)	GOF	Average crystallite size (nm)
$ZnCo_2O_4$	8.0874	13.90	2.55	1.17	51.3
$Mn_{0.3}Zn_{0.7}Co_2O_4$	8.1051	13.06	3.47	1.17	36.8
$Mn_{0.5}Zn_{0.5}Co_2O_4$	8.1241	14.29	2.40	1.09	19.9
$Mn_{0.7}Zn_{0.3}Co_2O_4$	8.1349	15.48	2.74	1.16	26.7
$MnCo_2O_4$	8.1508	14.49	2.85	1.11	19.3

FTIR spectroscopy is an important technique to identify the stretching and bending vibrations of different materials. Fig. 4 shows FTIR spectra in the range from 1000 to 400 cm^{-1} as signals in this range are generally attributed to the vibration bands of metallic ions in the crystal lattice. Two intense peaks were observed between 700 and 550 cm^{-1} for each $Mn_xZn_{1-x}Co_2O_4$ ($x = 0$, 0.3, 0.5, 0.7 and 1) sample, with a specific shift depending on Mn substitution (x). $ZnCo_2O_4$ ($x = 0$) exhibited absorption peaks centered at 677 and 585 cm^{-1} characteristic of Co–O and Zn–O vibration in the octahedral and tetrahedral sites of the spinel structure, respectively.[36] On doping $ZnCo_2O_4$ with Mn, the Mn ions replace Zn^{2+} from the tetrahedral site as it is evident from the change in the lattice parameter shown in the Rietveld refinement of XRD data, and the bands shift to higher wavenumbers, as seen in Fig. 4. For $MnCo_2O_4$ ($x = 1$), the peaks shift to 648 and 560 cm^{-1} compared to the undoped $ZnCo_2O_4$. This behaviour suggests changes in bonding occurs in the crystal structure, which could be affected by the ratio between Zn and Mn and the lighter atomic mass of Mn compared to that of Zn.[29] These observations further support the formation of cubic spinel crystal structure in the fabricated $Mn_xZn_{1-x}Co_2O_4$.

XPS measurements were performed in order to study the composition and investigate the electronic structure of the $Mn_xZn_{1-x}Co_2O_4$ series. Fig. 5(a) shows the full survey spectra for the five investigated samples. The spectra show all the expected peaks and no additional elements were detected. Photoemission and Auger peaks are labeled accordingly in the figure. Zn and Mn core levels vary in intensity according to the sample composition, as expected.

Fig. 5(b) shows the comparison of Mn 2p XPS core level spectra. Two main peaks with centroids at about 642 eV and 653.5 eV binding energy are visible in this energy region. These correspond to Mn $2p_{3/2}$ and $2p_{1/2}$ levels, respectively. The line shape of the main peaks remains identical across the series, indicating that there is no appreciable change in the valence of Mn with substitution by Zn. The only detectable difference is that the centroid of the satellite at the higher binding energy side of the $2p_{1/2}$ peak shifts by about 1.9 eV towards lower binding energies from $x = 0$ to $x = 0.7$ (the corresponding satellite for the $2p_{3/2}$ peak is not visible because it overlaps with the $2p_{1/2}$ peak). This is possibly due to the doping of the samples, as already reported for doped manganites.[37] Because of the fact that the line shape of the main peaks does not change, only the fit of the $x = 0$ sample at the bottom of Fig. 5(b) is reported. The Mn core level line shape was deconvoluted using two spin orbit doublets representing Mn^{2+} (at lower binding energy) and Mn^{3+} (at higher binding energy) respectively, separated by a spin orbit splitting of 11.2 eV. The area ratio of these two doublets shows that roughly 55% of the Mn ions have a 2+ ionization state and 45% have a 3+ ionization state.

Zn 2p core level spectra for samples $x = 0.3$, 0.5 and 0.7 are reported in Fig. 5(c). The line shape is composed of two peaks at 1021.1 eV and 1044.2 eV, corresponding to Zn $2p_{3/2}$ and $2p_{1/2}$ spin orbit components, respectively. The line shape remains the same for the three compositions. This is consistent with Zn ions being found in +2 oxidation state, as reported in previous works.[38,39]

Fig. 5(d) reports the Co 2p XPS spectra for $Mn_xZn_{1-x}Co_2O_4$. The Co 2p binding energy region is composed of two main peaks located at 780.2 eV and 795.3 eV, corresponding to the Co $2p_{3/2}$ and Co $2p_{1/2}$ spin–orbit components, respectively. In addition to these, two satellite peaks are detected on the higher binding energy of the main peaks. The line shape of the Co 2p spectrum shows changes across the series. For this reason, the spectra for $MnCo_2O_4$ and $Zn_{0.7}Mn_{0.3}Co_2O_4$ are plotted separately in Fig. 5(e), together with the overall fit to the data. The spectra have been decomposed into two main doublets corresponding to Co^{3+} (at lower binding energy) and Co^{2+} (at higher

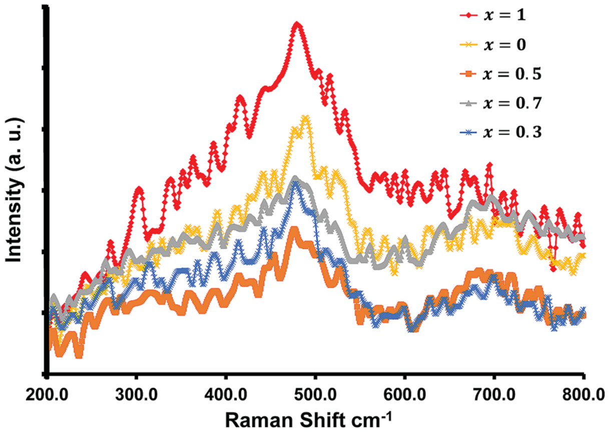

Fig. 3 Raman spectra of various concentration of Mn doped $ZnCo_2O_4$.

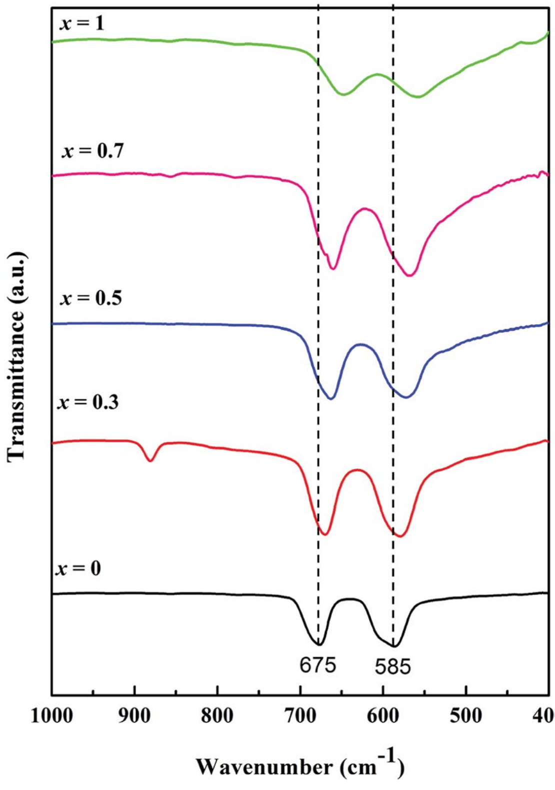

Fig. 4 FTIR spectra of the Mn substituted $Mn_xZn_{1-x}Co_2O_4$ oxide with different Mn concentrations; $x = 0$, 0.3, 0.5, 0.7 and 1.

binding energy) oxidation states. The satellite has been fitted with a broad doublet. It is interesting to note that the percentage of Co^{3+} spectral weight increases from 76% in $MnCo_2O_4$ to 84% in $Zn_{0.7}Mn_{0.3}Co_2O_4$. This shows that the Co^{3+} content is slightly higher than in similar oxide systems.[40,41] At the same time, the centroid of the satellite doublet shifts to 4 eV higher binding energy and becomes much narrower when moving from $MnCo_2O_4$ to $Zn_{0.7}Mn_{0.3}Co_2O_4$.

The ratio of Co^{3+}/Co^{2+} ions present in the $Mn_xZn_{1-x}Co_2O_4$ oxides can be determined from the deconvoluted high resolution Co 2p spectrum and is given in Table 2. For the prepared samples, with increase in manganese concentration Co^{3+}/Co^{2+} ratio increases, which are consistent with previously reported literatures.[42,43]

Fig. 5(f) shows the O 1s XPS spectra for the series. Each spectrum has been fitted with three Voigt-type single

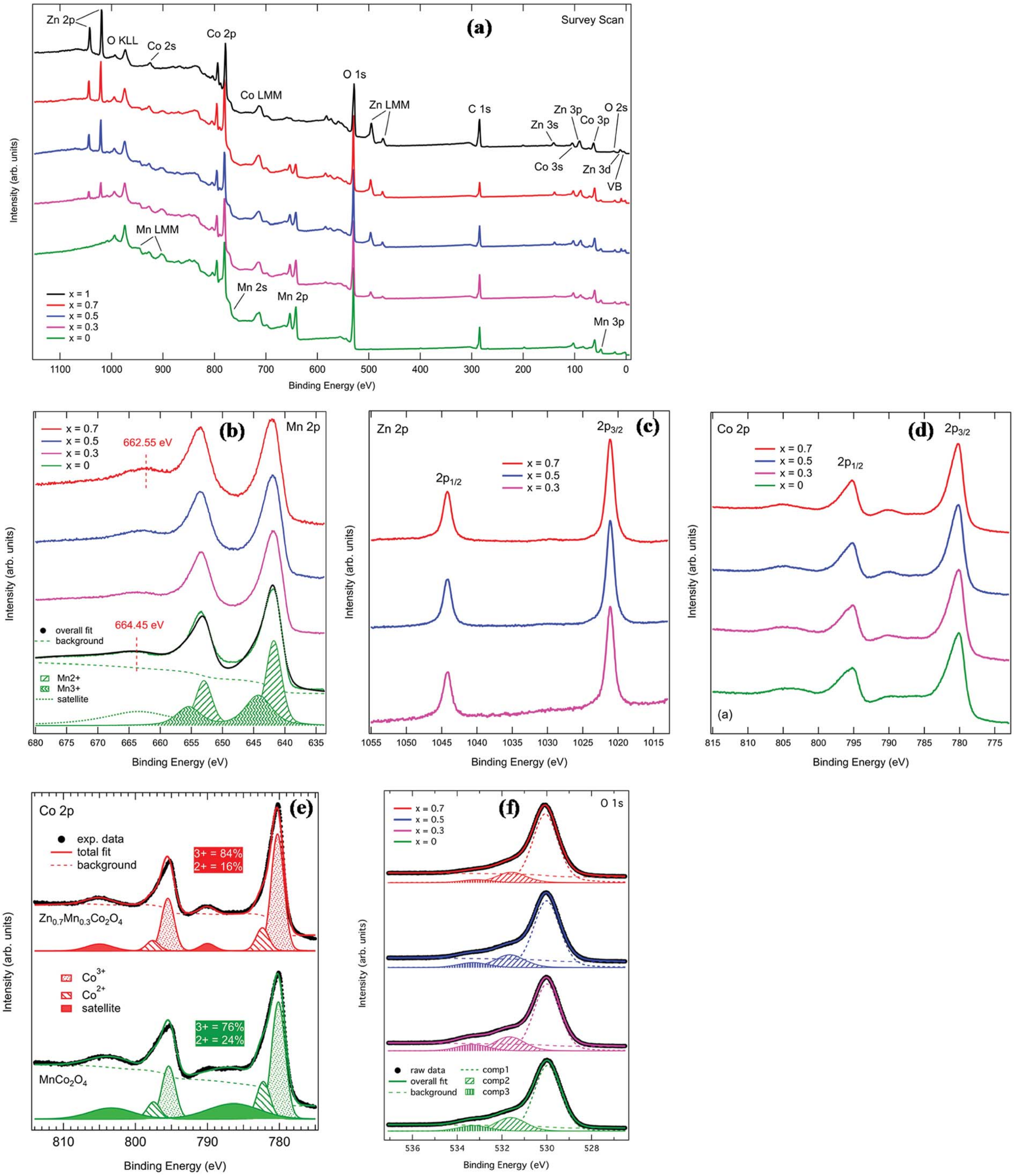

Fig. 5 (a) XPS survey scans for the investigated samples. (b) Mn 2p core level spectra for $x = 0.3$, 0.5, 0.7, and 1 samples (c) Zn 2p spectra for $x = 0.3$, 0.5 and 0.7 samples (d) Co 2p core level spectra for $Mn_xZn_{1-x}Co_2O_4$ spinel oxides. (e) Fitted Co 2p spectra for $MnCo_2O_4$ and $Zn_{0.7}Mn_{0.3}Co_2O_4$ and (f) O 1s core level spectra for $Mn_xZn_{1-x}Co_2O_4$ spinel oxides.

Table 2 Oxidation state ratios obtained by deconvoluting XPS peaks corresponding to Co 2p and Mn 2p core electrons

	Oxidation states ratios obtained from XPS	
$Mn_xZn_{1-x}Co_2O_4$	Co^{3+}/Co^{2+}	Mn^{3+}/Mn^{2+}
$x = 0.3$	5.25	0.82
$x = 0.5$	4.55	0.82
$x = 0.7$	3.87	0.82
$x = 1$	3.17	0.82

components (labeled as "comp1", "comp2" and "comp3" in the figure) in addition to a Shirley background. This is consistent with what has been published in the literature for similar systems.[40,41] Component 1, on the lower binding energy side, is ascribed to stoichiometric oxygen in the oxide main matrix, while the second component is attributed to oxygen vacancies or defects in the lattice.[41] The third component at 533 eV can be ascribed to chemisorbed oxygen.[44] The fitted binding energies and relative percentage areas of these three components are reported in Table 3. In general, the fit results show that there is no significant change in the line shape of O 1s spectra across the series.

3.3 Morphological characterization

Fig. 6(a) through Fig. 6(e) presents the SEM images of the $Mn_xZn_{1-x}Co_2O_4$ (x = 0, 0.3, 0.5, 0.7, 1) while Fig. 5(f) is EDS spectrum of the $Mn_{0.5}Zn_{0.5}Co_2O_4$ sample. Microspheres of different size with varying concentration of Mn have been obtained as observed from the SEM images. The size of the microspheres tends to increase and become more regular with increasing concentration of Mn from $x = 0$ to $x = 1$. The results indicate that Mn content plays an important role in determining the surface morphologies of $Mn_xZn_{1-x}Co_2O_4$ microstructure. The EDS analysis of the $Mn_{0.5}Zn_{0.5}Co_2O_4$ sample in Fig. 5(f) shows that the main elements in the sample are

Table 3 Fit results for O 1s core level

Sample	BE comp1 (eV)	BE comp2 (eV)	BE comp3 (eV)	% area (comp1)	% area (comp2)	% area (comp3)
$x = 0$	529.97	531.61	533.27	74.9	17.8	7.3
$x = 0.3$	530.02	531.67	533.31	73.4	18.3	8.3
$x = 0.5$	530.01	531.65	533.29	76.7	16.7	6.6
$x = 0.7$	530.07	531.58	533.12	81.2	14.6	4.2

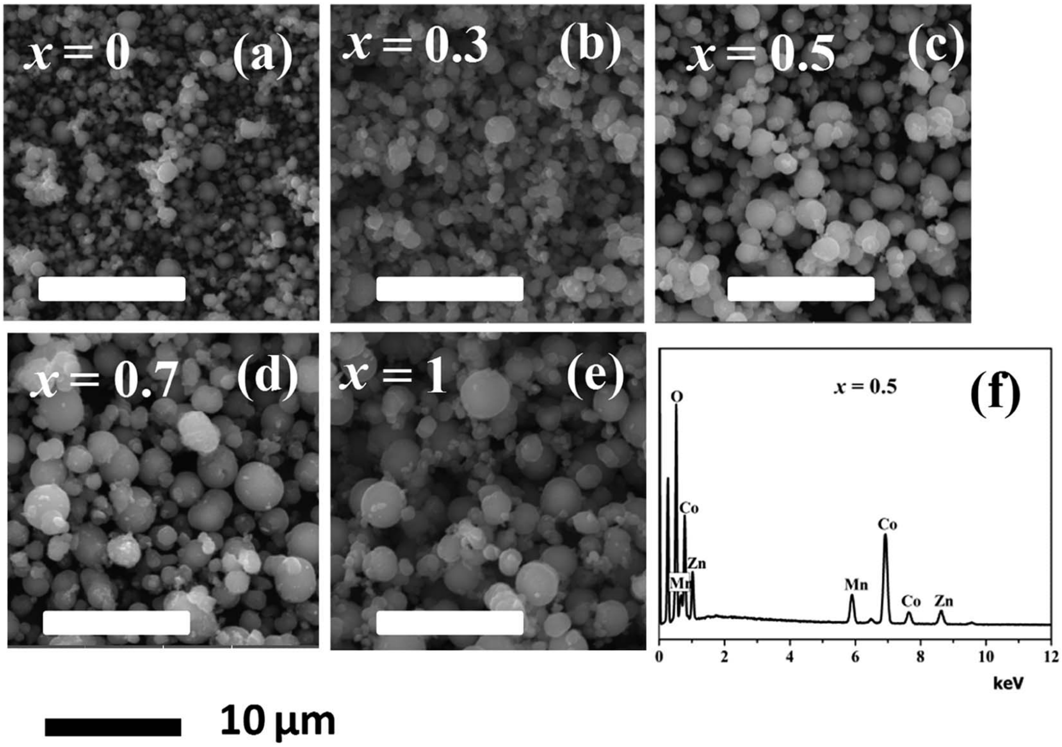

Fig. 6 SEM images of the $Mn_xZn_{1-x}Co_2O_4$ microspheres (x = 0, 0.3, 0.5, 0.7, 1) (a–e), and (f) EDS spectrum of the $Mn_{0.5}Zn_{0.5}Co_2O_4$ ($x = 0.5$) sample.

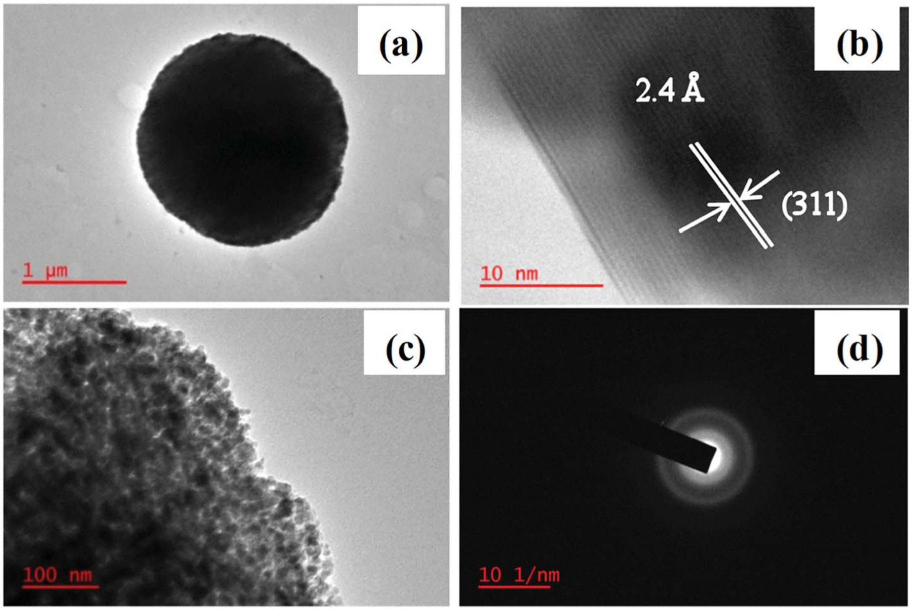

Fig. 7 (a) TEM, (b) HRTEM (c) magnified TEM and (d) SAED pattern of the $Mn_{0.5}Zn_{0.5}Co_2O_4$ ($x = 0.5$) microsphere.

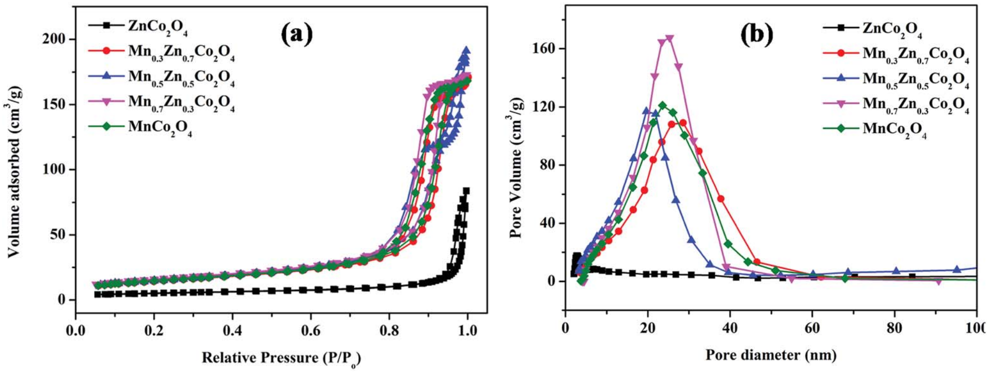

Fig. 8 Nitrogen adsorption/desorption isotherms (a) and the corresponding pore size distributions (b) of the $Mn_xZn_{1-x}Co_2O_4$ ($x = 0, 0.3, 0.5, 0.7, 1$) samples.

manganese, zinc, cobalt, and oxygen and that the approximate atomic ratio of Mn/Zn/Co is about 1 : 0.97 : 2.1.

Representative TEM, HRTEM, and SAED images of $Mn_{0.5}Zn_{0.5}Co_2O_4$ microspheres are shown in Fig. 7. The TEM image demonstrates the porous nature of the microspheres and it is made up of small interconnected nanoparticles as shown by the magnified TEM image (Fig. 7(c)). Clearly, the corresponding selected-area electron diffraction (SAED) pattern displays the diffraction rings, indicating that the porous $Mn_{0.5}Zn_{0.5}Co_2O_4$ microspheres are polycrystalline (Fig. 7(d)). The HRTEM image (Fig. 7(b)) further confirms the high crystallinity of the porous $Mn_{0.5}Zn_{0.5}Co_2O_4$ microspheres. The lattice fringe with a spacing of ~2.4 Å is assigned to the interplanar spacing between the (311) planes of cubic $Mn_{0.5}Zn_{0.5}Co_2O_4$.

The specific surface areas and pore size distribution of $Mn_xZn_{1-x}Co_2O_4$ oxides were characterized by BET analysis using nitrogen adsorption–desorption isotherms. The N_2 adsorption–desorption isotherms and pore size distribution data for $Mn_xZn_{1-x}Co_2O_4$ ($x = 0, 0.3, 0.5, 0.7, 1$) samples are shown in Fig. 8. As shown in the Fig. 8(a), the N_2 adsorption–desorption isotherms obtained for the $Mn_xZn_{1-x}Co_2O_4$ are type IV, according to the IUPAC classification of hysteresis loops.[45] Distinct H3 hysteresis loops were observed at a relative pressure of $P/P_o = 0.8–1.0$ except for $ZnCo_2O_4$, indicating the mesoporous structure of $Mn_xZn_{1-x}Co_2O_4$ microspheres.[46] The textural properties of the samples are given in Table 4. It can be seen that the BET surface areas of 17.8, 50.25, 51.47, 56.27, and

Table 4 Textural properties of $Mn_xZn_{1-x}Co_2O_4$ samples

Sample	BET surface area ($m^2\ g^{-1}$)	Pore volume ($cm^3\ g^{-1}$)	Average pore size (nm)
$ZnCo_2O_4$	17.80	0.00563	36.0
$Mn_{0.3}Zn_{0.7}Co_2O_4$	50.25	0.01280	19.4
$Mn_{0.5}Zn_{0.5}Co_2O_4$	51.47	0.01461	20.0
$Mn_{0.7}Zn_{0.3}Co_2O_4$	56.27	0.01353	17.5
$MnCo_2O_4$	51.66	0.01171	18.4

51.66 $m^2\ g^{-1}$ were obtained for $ZnCo_2O_4$, $Mn_{0.3}Zn_{0.7}Co_2O_4$, $Mn_{0.5}Zn_{0.5}Co_2O_4$, $Mn_{0.7}Zn_{0.3}Co_2O_4$, and $MnCo_2O_4$, respectively. It was observed that the BET surface area increases with substitution of Zn by Mn. This modification of the surface area correlates with the change in microsphere size as shown on the SEM images. The pore size distributions were mainly centered between 20 and 30 nm with an average pore diameter of 36, 19.4, 20, 17.5, and 18.4 nm, mainly resulting from the aggregation among primary particles as is evident from the TEM image.

3.4 Magnetic properties

The magnetic properties of $Mn_xZn_{1-x}Co_2O_4$ samples were examined using a vibrating sample magnetometer (VSM) at room temperature and 10 K by applying a magnetic field of ±25 kOe. Magnetic hysteresis loops and the temperature dependent zero-field-cooled (ZFC) and field-cooled (FC) curves are shown in Fig. 9 and 10, respectively.

Temperature dependent magnetization curves $M(T)$ were collected under the zero field cooled (ZFC) and field cooled (FC) conditions and measured in the temperature range 2–300 K at 500 Oe. The magnetization during FC for all samples shows a general increase with decreasing temperature. However, it is noted that as the Mn concentration is increased the FC data tends to level of at low temperatures and an additional inflection similar to the peaks observed in the ZFC $M(T)$ data develops. All the samples exhibit distinct bifurcation between ZFC and FC, except $ZnCo_2O_4$ ($x = 0$) for which the zero-field cooled and field cooled (ZFC-FC) curves did not diverge. The bifurcation temperature increases with an increase in Mn doping.

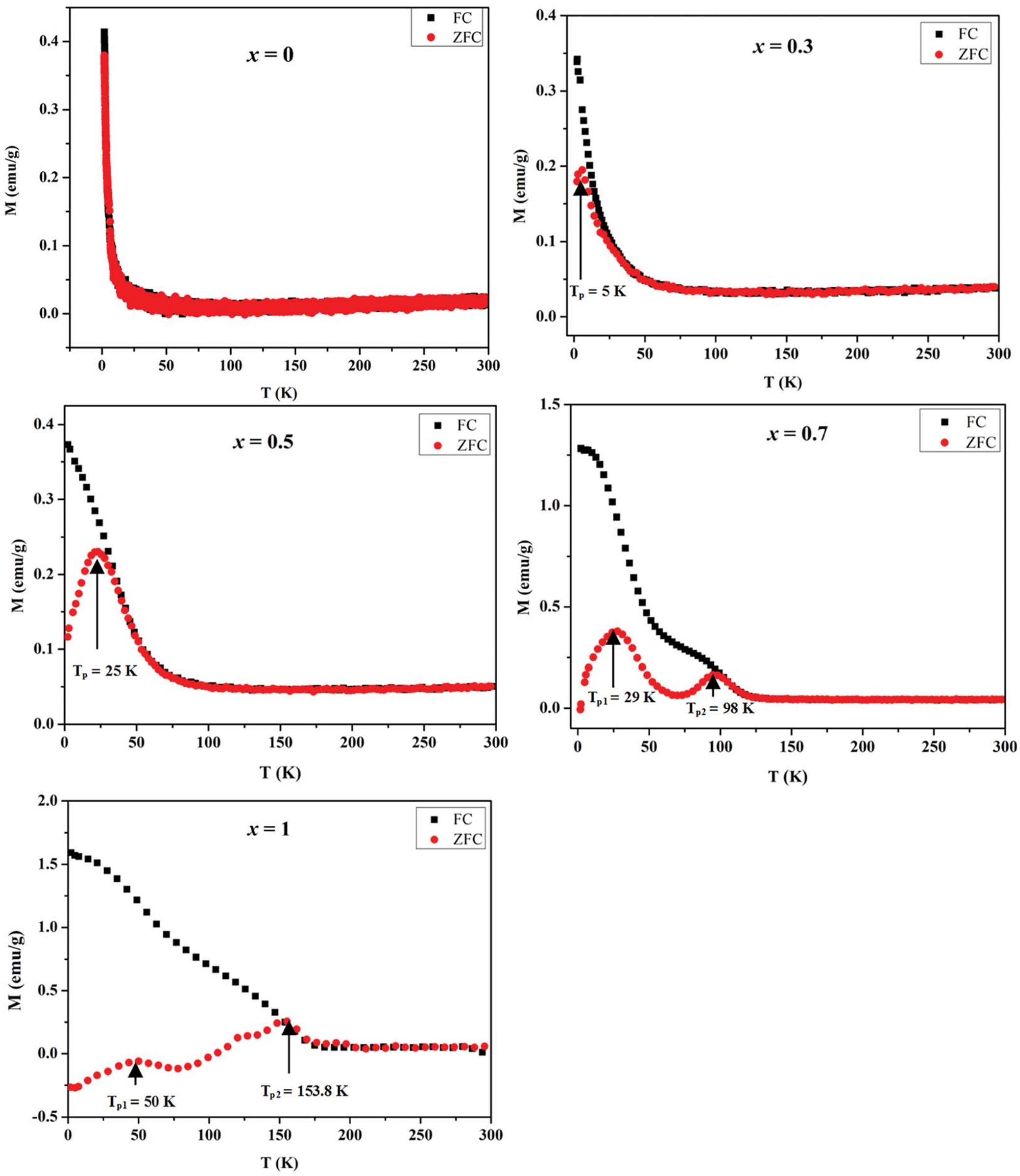

Fig. 9 Temperature dependent ZFC and FC magnetization of $Mn_xZn_{1-x}Co_2O_4$ microspheres with different concentration of Mn ($x = 0$, 0.3, 0.5, 0.7, 1) measured at an applied field of 500 Oe.

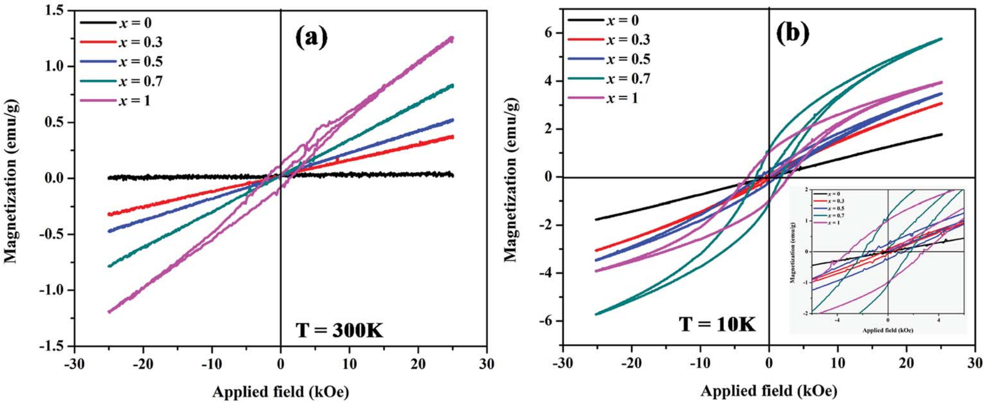

Fig. 10 Magnetic hysteresis loops of $Mn_xZn_{1-x}Co_2O_4$ microspheres with different concentration of Mn ($x = 0, 0.3, 0.5, 0.7, 1$) measured at (a) 300 K and (b) 10 K.

Generally, the presence of a maximum temperature (T_{max}) in the ZFC magnetization curve is directly proportional to the average blocking temperature (T_B) that depends upon the type of size distribution. The temperatures associated with the maxima in the ZFC magnetization data for the prepared $Mn_xZn_{1-x}Co_2O_4$ samples is observed at $T_P = 5.5$ K for $x = 0.3$, $T_P = 25$ K for $x = 0.5$, $T_{P1} = 29$ K and $T_{P2} = 98$ K for $x = 0.7$, and $T_{P1} = 50$ K and $T_{P2} = 153.8$ K for $x = 1$. It is clear from these data that as more of Zn is substituted by Mn, the T_P values increase and eventually more than one T_P values are observed for $x = 0.7$ and 1, which may well be a result of the substitution of nonmagnetic Zn^{2+} by the Mn^{2+}/Mn^{3+} ions.[47] On moving form $x = 0.7$ to $x = 1.0$ the magnetization is suppressed to negative values below a temperature of approximately 100 K. This is due to a compensation effect, as the net magnetization is dependent on the sum of the magnetic contributions from the associated sublattices within the spinel structure.[48]

Fig. 10 shows magnetic hysteresis loops of $Mn_xZn_{1-x}Co_2O_4$ ($x = 0, 0.3, 0.5, 0.7, 1$) microspheres measured at temperatures of 10 K and 300 K. The magnetization as a function of applied magnetic field, *M–H*, curves shows hysteretic behavior in all samples at 10 K, with the exception of the $ZnCo_2O_4$ sample. The magnetization is not fully saturated in fields of 25 kOe in all samples measured at 10 K, which represents the weak ferromagnetic ordering of the spins. The saturation magnetization for the samples was determined from extrapolation of *M versus* 1/*H* curve at $1/H = 0$. The saturation magnetization (M_s), remnant magnetization (M_r), and coercive field (H_c) are summarized in Table 5. The M_s gradually increases from 0.01 ($x = 0$) to 1.3 ($x = 1$) emu/g and 1.82 ($x = 0$) to 5.92 ($x = 0.7$) emu g^{-1} measured at 300 K and 10 K, respectively with increasing Mn concentrations. The maximum value of H_c is observed for $x = 1$ ($MnCo_2O_4$).

M–H measurements done at 300 K shown in Fig. 10(a) reflects linear behavior associated with paramagnetism for all the samples, with the exception of the $MnCo_2O_4$ ($x = 1$) sample. For this sample weak hysteresis is still observed, thus indicating the antiferromagnetic nature of this sample at 300 K.[43,49] This type of behavior is observed for Cu substituted spinel $MnCo_{2-x}Cu_xO_4$ ($0 \leq x \leq 0.2$) nanostructures with the samples $x \geq 0.1$ having the coercivity H_c and remanence M_r close to 0.[50]

In the $Mn_xZn_{1-x}Co_2O_4$ the non-magnetic divalent Zn^{2+} ions tend to occupy tetrahedral (A) sites and thereby force the incoming Mn ions to octahedral (B) sites due to their favoritism by polarization effect.[30] In general, spinel type cobalt-based oxides contain high spin Co^{2+} ($S = 3/2$) in the tetrahedral site and low spin diamagnetic Co^{3+} ($S = 0$) in the octahedral site; magnetic ions in the sub lattices are arranged antiparallel to their four neighboring ions resulting in antiferromagnetic behavior of the material.[51] In view of the above considerations and the ratio Co^{3+}/Co^{2+} given in the Table 2 it can be shown that there is an enhancement of weak ferromagnetism of the samples with substitution of Zn with Mn ions. $ZnCo_2O_4$ is observed to have a linear *M–H* curve both at room temperature and 10 K, which is typical of paramagnetic nature and results due to Co–O–Co super exchange interaction.[22,23] As the content of Mn ions increase and with both Mn^{2+} and Mn^{3+} distributed in the octahedral and tetrahedral sites, the magnetic moment

Table 5 Magnetic parameters for $Mn_xZn_{1-x}Co_2O_4$ samples measured at temperatures of 300 K and 10 K

	300 K			10 K		
Sample	M_s (emu g^{-1})	M_r (emu g^{-1})	H_c (kOe)	M_s (emu g^{-1})	M_r (emu g^{-1})	H_c (kOe)
$ZnCo_2O_4$	0.01	0	0	1.82	0	0
$Mn_{0.3}Zn_{0.7}Co_2O_4$	0.4	0	0	3.15	0.07	0.3
$Mn_{0.5}Zn_{0.5}Co_2O_4$	0.55	0	0	3.51	0.25	1.32
$Mn_{0.7}Zn_{0.3}Co_2O_4$	0.87	0	0	5.92	1.15	1.93
$MnCo_2O_4$	1.3	0.12	1.2	4.08	1.03	3.02

on B-site increases and the magnetic moment on A-sites decreases and it leads to a stronger superexchange interaction between A and B sites. Thus, the net value of M_s increases, as expected.

4. Conclusions

$Mn_xZn_{1-x}Co_2O_4$ oxide microspheres with a spinel structure were successfully prepared by using a facile coprecipitation method and calcination. It formed porous microspheres with the surface area and morphology being influenced by the composition of Mn. The lattice parameters for the spinel oxides increased linearly with Mn concentration. The results from XPS indicates that the elements Mn, Zn, and Co are observed to have oxidation states of +2 and +3, +2, and +2 and +3, respectively. It was shown that the percentage of Co^{3+} spectral weight increases from 76% in $MnCo_2O_4$ to 84% in $Zn_{0.7}Mn_{0.3}Co_2O_4$ whereas no appreciable change in the valence of Mn was observed with substitution by Zn. The magnetic properties of the $Mn_xZn_{1-x}Co_2O_4$ microspheres are largely influenced by the concentration of Mn. As the concentration of Mn increases from $x = 0$ to $x = 1$ the saturation magnetization increases from 0.01 ($x = 0$) to 1.3 ($x = 1$) emu g^{-1} and 1.82 ($x = 0$) to 5.92 ($x = 0.7$) emu g^{-1} measured at 300 K and 10 K, respectively, which could be due to the substitution of the non-magnetic Zn^{2+} ion by Mn ions. The $MnCo_2O_4$ microspheres show maximum H_c of 1.2 and 3.02 kOe measured at 300 K and 10 K, respectively.

Conflicts of interest

There are no conflicts to declare.

Acknowledgements

The work reported herein was partially funded the National Research Foundation (South Africa), Grant numbers: 88080, 109623, and 93620. In addition, the authors thank the Centre for Nanomaterials Science Research at the Department of Applied Chemistry, the Department of Physics, the Faculty of Science at University of Johannesburg, and the School of Chemistry at University of the Witwatersrand, for support and access to research facilities.

References

1 X. Niu, W. Du and W. Du, Preparation and gas sensing properties of ZnM_2O_4 (M = Fe, Co, Cr), *Sens. Actuators, B*, 2004, **99**(2–3), 405–409.

2 H. J. Park, J. Kim, N.-J. Choi, H. Song and D.-S. Lee, Nonstoichiometric Co-rich $ZnCo_2O_4$ hollow nanospheres for high performance formaldehyde detection at ppb levels, *ACS Appl. Mater. Interfaces*, 2016, **8**(5), 3233–3240.

3 M.-S. Park, J. Kim, K. J. Kim, J.-W. Lee, J. H. Kim and Y. Yamauchi, Porous nanoarchitectures of spinel-type transition metal oxides for electrochemical energy storage systems, *Phys. Chem. Chem. Phys.*, 2015, **17**(46), 30963–30977.

4 C. Lin, Y. Li, M. Yu, P. Yang and J. Lin, A facile synthesis and characterization of monodisperse spherical pigment particles with a core/shell structure, *Adv. Funct. Mater.*, 2007, **17**(9), 1459–1465.

5 K. Omata, T. Takada, S. Kasahara and M. Yamada, Active site of substituted cobalt spinel oxide for selective oxidation of COH_2. Part II, *Appl. Catal., A*, 1996, **146**(2), 255–267.

6 E. Kan, M. Li, S. Hu, C. Xiao, H. Xiang and K. Deng, Two-dimensional hexagonal transition-metal oxide for spintronics, *J. Phys. Chem. Lett.*, 2013, **4**(7), 1120–1125.

7 J.-M. Li, A. C. H. Huan, L. Wang, Y.-W. Du and D. Feng, Interface effects on magnetoresistance and magnetic-field-reduced Raman scattering in magnetite, *Phys. Rev. B: Condens. Matter Mater. Phys.*, 2000, **61**(10), 6876–6878.

8 L. Wang, J. Li, W. Ding, T. Zhou, B. Liu, W. Zhong, J. Wu and Y. Du, Magnetoelectric transport properties of quenched polycrystalline magnetite, *J. Magn. Magn. Mater.*, 1999, **207**(1), 111–117.

9 Y. Qiu, S. Yang, H. Deng, L. Jin and W. Li, A novel nanostructured spinel $ZnCo_2O_4$ electrode material: morphology conserved transformation from a hexagonal shaped nanodisk precursor and application in lithium ion batteries, *J. Mater. Chem.*, 2010, **20**(21), 4439–4444.

10 S. Vijayanand, P. A. Joy, H. S. Potdar, D. Patil and P. Patil, Nanostructured spinel $ZnCo_2O_4$ for the detection of LPG, *Sens. Actuators, B*, 2011, **152**(1), 121–129.

11 T. W. Kim, M. A. Woo, M. Regis and K.-S. Choi, Electrochemical synthesis of spinel type $ZnCo_2O_4$ electrodes for use as oxygen evolution reaction catalysts, *J. Phys. Chem. Lett.*, 2014, **5**(13), 2370–2374.

12 H. Guo, J. Chen, W. Weng, Q. Wang and S. Li, Facile template-free one-pot fabrication of $ZnCo_2O_4$ microspheres with enhanced photocatalytic activities under visible-light illumination, *Chem. Eng. J.*, 2014, **239**, 192–199.

13 S. Wang, Z. Ding and X. Wang, A stable $ZnCo_2O_4$ cocatalyst for photocatalytic CO_2 reduction, *Chem. Commun.*, 2015, **51**(8), 1517–1519.

14 F.-L. Schein, H. von Wenckstern, H. Frenzel and M. Grundmann, ZnO-Based n-Channel Junction Field-Effect Transistor With Room-Temperature-Fabricated Amorphous p-Type $ZnCo_2O_4$ Gate, *IEEE Electron Device Lett.*, 2012, **33**(5), 676–678.

15 B. Henne, V. Ney, K. Ollefs, F. Wilhelm, A. Rogalev and A. Ney, Magnetic interactions in the ZnCoO system: tuning local structure, valence and carrier type from extremely Co doped ZnO to $ZnCo_2O_4$, *Sci. Rep.*, 2015, **5**, 16863.

16 P. Sati, C. Deparis, C. Morhain, S. Schäfer and A. Stepanov, Antiferromagnetic interactions in single crystalline $Zn_{1-x}Co_xO$ thin films, *Phys. Rev. Lett.*, 2007, **98**(13), 137204.

17 X. Wen, Z. Chen, E. Liu and X. Lin, Structural and magnetic characterization of $ZnCo_2O_4$ thin film prepared by pulsed laser deposition, *Appl. Surf. Sci.*, 2015, **357**, 1212–1216.

18 T. Kammermeier, V. Ney, S. Ye, K. Ollefs, T. C. Kaspar, S. A. Chambers, F. Wilhelm, A. Rogalev and A. Ney, Element specific measurements of the structural properties and magnetism of $Co_xZn_{1-x}O$, *J. Magn. Magn. Mater.*, 2009, **321**(7), 699–701.

19 R. Khan, C. I. L. de Araujo, T. Khan, A. Khan, B. Ullah and S. Fashu, Influence of oxygen vacancies on the structural, dielectric, and magnetic properties of (Mn, Co) co-doped ZnO nanostructures, *J. Mater. Sci.: Mater. Electron.*, 2018, **29**(12), 9785–9795.

20 S.-g. Kang, Y. Kim, S. E. Kim and S. Kim, The effects of heat treatment on room temperature ferromagnetism in a digitally Co doped ZnO thin film, *Electron. Mater. Lett.*, 2013, **9**(1), 7–11.

21 M. Shatnawi, A. M. Alsmadi, I. Bsoul, B. Salameh, M. Mathai, G. Alnawashi, G. M. Alzoubi, F. Al-Dweri and M. S. Bawa'aneh, Influence of Mn doping on the magnetic and optical properties of ZnO nanocrystalline particles, *Results Phys.*, 2016, **6**, 1064–1071.

22 H. J. Kim, I. C. Song, J. H. Sim, H. Kim, D. Kim, Y. E. Ihm and W. K. Choo, Electrical and magnetic properties of spinel-type magnetic semiconductor $ZnCo_2O_4$ grown by reactive magnetron sputtering, *J. Appl. Phys.*, 2004, **95**(11), 7387–7389.

23 M. Baskey, R. Maiti, S. Kumar Saha and D. Chakravorty, Superior magnetic, dielectric, and magnetodielectric effects in graphene/$ZnCo_2O_4$ nanocomposites, *J. Appl. Phys.*, 2014, **115**(9), 094306.

24 J. H. Kim, H. Kim, D. Kim, Y. E. Ihm and W. K. Choo, Magnetoresistance in laser-deposited $Zn_{1-x}Co_xO$ thin films, *Phys. B*, 2003, **327**(2–4), 304–306.

25 H. J. Kim, I. C. Song, J. H. Sim, H. Kim, D. Kim, Y. E. Ihm and W. K. Choo, Growth and characterization of spinel-type magnetic semiconductor $ZnCo_2O_4$ by reactive magnetron sputtering, *Phys. Status Solidi B*, 2004, **241**(7), 1553–1556.

26 N. H. Perry, T. O. Mason, C. Ma, A. Navrotsky, Y. Shi, J. S. Bettinger, M. F. Toney, T. R. Paudel, S. Lany and A. Zunger, Co_3O_4–Co_2ZnO_4 spinels: The case for a solid solution, *J. Solid State Chem.*, 2012, **190**, 143–149.

27 S. Maria and S. L. Cynthia, P-type zinc oxide spinels: application to transparent conductors and spintronics, *New J. Phys.*, 2014, **16**(5), 055011.

28 D. S. Nikam, S. V. Jadhav, V. M. Khot, R. Bohara, C. K. Hong, S. S. Mali and S. Pawar, Cation distribution, structural, morphological and magnetic properties of $Co_{1-x}Zn_xFe_2O_4$ ($x = 0$–1) nanoparticles, *RSC Adv.*, 2015, **5**(3), 2338–2345.

29 N. Wiriya, A. Bootchanont, S. Maensiri and E. Swatsitang, Magnetic properties of $Zn_{1-x}Mn_xFe_2O_4$ nanoparticles prepared by hydrothermal method, *Microelectron. Eng.*, 2014, **126**, 1–8.

30 L. Hao, Y. Zhao, Q. Jiao and P. Chen, Synthesis of zinc–nickel ferrite nanorods and their magnetic properties, *RSC Adv.*, 2014, **4**(30), 15650–15654.

31 R. D. Shannon, Revised Effective Ionic Radii and Systematic Studies of Interatomic Distances in Halides and Chalcogenides, *Acta Crystallogr.*, 1976, **A32**, 751.

32 M. Bouchard and A. Gambardella, Raman microscopy study of synthetic cobalt blue spinels used in the field of art, *J. Raman Spectrosc.*, 2010, **41**(11), 1477–1485.

33 B. Hadžić, N. Romčević, M. Romčević, I. Kuryliszyn-Kudelska, W. D. Dobrowolski, U. Narkiewicz and D. Sibera, Raman study of surface optical phonons in ZnO (Co) nanoparticles prepared by hydrothermal method, *Hem. Ind.*, 2013, **67**(4), 695–701.

34 K. K. Naik and C. S. Rout, Electrodeposition of $ZnCo_2O_4$ nanoparticles for biosensing applications, *RSC Adv.*, 2015, **5**(97), 79397–79404.

35 C. Stella, N. Soundararajan and K. Ramachandran, Structural, optical, and magnetic properties of Mn and Fe-doped Co_3O_4 nanoparticles, *AIP Adv.*, 2015, **5**(8), 087104.

36 L. Lu, S. Xu, Z. Luo, S. Wang, G. Li and C. Feng, Synthesis of $ZnCo_2O_4$ microspheres with $Zn_{0.33}Co_{0.67}CO_3$ precursor and their electrochemical performance, *J. Nanopart. Res.*, 2016, **18**(7), 183.

37 K. Garg, P. Nordblad, M. Heinonen, N. Panwar, V. Sen, F. Bondino, E. Magnano, E. Carleschi, F. Parmigiani and S. Agarwal, Study of Sb substitution for Pr in the $Pr_{0.67}Ba_{0.33}MnO_3$ system, *J. Magn. Magn. Mater.*, 2009, **321**(4), 305–311.

38 J. Zheng, Q. Jiang and J. Lian, Synthesis and optical properties of flower-like ZnO nanorods by thermal evaporation method, *Appl. Surf. Sci.*, 2011, **257**(11), 5083–5087.

39 M. Ahmed, B. S. Mwankemwa, E. Carleschi, B. Doyle, W. E. Meyer and J. M. Nel, Effect of Sm doping ZnO nanorods on structural optical and electrical properties of Schottky diodes prepared by chemical bath deposition, *Mater. Sci. Semicond. Process.*, 2018, **79**, 53–60.

40 D. McNulty, H. Geaney and C. O'Dwyer, Carbon-coated honeycomb Ni–Mn–Co–O inverse opal: a high capacity ternary transition metal oxide anode for Li-ion batteries, *Sci. Rep.*, 2017, **7**, 42263.

41 T. H. Dolla, K. Pruessner, D. G. Billing, C. Sheppard, A. Prinsloo, E. Carleschi, B. Doyle and P. Ndungu, Sol-gel synthesis of $Mn_xNi_{1-x}Co_2O_4$ spinel phase materials: Structural, electronic, and magnetic properties, *J. Alloys Compd.*, 2018, **742**, 78–89.

42 Q. Zhang, X. Liu, W. Fan and Y. Wang, Manganese-promoted cobalt oxide as efficient and stable non-noble metal catalyst for preferential oxidation of CO in H_2 stream, *Appl. Catal., B*, 2011, **102**(1–2), 207–214.

43 A. N. Naveen and S. Selladurai, Tailoring structural, optical and magnetic properties of spinel type cobalt oxide (Co_3O_4) by manganese doping, *Phys. B*, 2015, **457**, 251–262.

44 A. Pendashteh, J. Palma, M. Anderson and R. Marcilla, Facile synthesis of $NiCoMnO_4$ nanoparticles as novel electrode materials for high-performance asymmetric energy storage devices, *RSC Adv.*, 2016, **6**(34), 28970–28980.

45 K. Sing, D. Everett, R. Haul, L. Moscou, L. Pierotti, J. Rouquerol and T. Siemieniewska, International union of pure and applied chemistry physical chemistry division reporting physisorption data for gas/soils systems with special reference to the determination of surface area and porosity, *Pure Appl. Chem.*, 1985, **57**, 603–619.

46 S. Storck, H. Bretinger and W. F. Maier, Characterization of micro-and mesoporous solids by physisorption methods and pore-size analysis, *Appl. Catal., A*, 1998, **174**(1–2), 137–146.

47 S. Yang and Y. Zhang, Structural, optical and magnetic properties of Mn-doped ZnO thin films prepared by sol–gel method, *J. Magn. Magn. Mater.*, 2013, **334**, 52–58.

48 D. P. Dutta, J. Manjanna and A. Tyagi, Magnetic properties of sonochemically synthesized $CoCr_2O_4$ nanoparticles, *J. Appl. Phys.*, 2009, **106**(4), 043915.

49 S. Singh, P. Pramanik, S. Sangaraju, A. Mallick, L. Giebeler and S. Thota, Size-dependent structural, magnetic, and optical properties of $MnCo_2O_4$ nanocrystallites, *J. Appl. Phys.*, 2017, **121**(19), 194303.

50 P. Pramanik, S. Thota, S. Singh, D. C. Joshi, B. Weise, A. Waske and M. Seehra, Effects of Cu doping on the electronic structure and magnetic properties of $MnCo_2O_4$ nanostructures, *J. Phys.: Condens. Matter*, 2017, **29**(42), 425803.

51 W. L. Roth, The magnetic structure of Co_3O_4, *J. Phys. Chem. Solids*, 1964, **25**(1), 1–10.